The Astrophysical Journal, 833:36 (8pp), 2016 December 10 doi:10.3847/1538-4357/833/1/36

THE ROLE OF KELVIN–HELMHOLTZ INSTABILITY FOR PRODUCING LOOP-TOP HARD X-RAY SOURCES IN SOLAR FLARES

Xia Fang, Ding Yuan, Chun Xia, Tom Van Doorsselaere, and Rony Keppens
Centre for Mathematical Plasma Astrophysics, Department of Mathematics, KU Leuven, Celestijnenlaan 200B, 3001 Leuven, Belgium
Received 2016 February 5; revised 2016 September 6; accepted 2016 October 9; published 2016 December 6

ABSTRACT

We propose a model for the formation of loop-top hard X-ray (HXR) sources in solar flares through the inverse Compton mechanism, scattering the surrounding soft X-ray (SXR) photons to higher energy HXR photons. We simulate the consequences of a flare-driven energy deposit in the upper chromosphere in the impulsive phase of single loop flares. The consequent chromosphere evaporation flows from both footpoints reach speeds up to hundreds of kilometers per second, and we demonstrate how this triggers Kelvin–Helmholtz instability (KHI) in the loop top, under mildly asymmetric conditions, or more toward the loop flank for strongly asymmetric cases. The KHI vortices further fragment the magnetic topology into multiple magnetic islands and current sheets, and the hot plasma within leads to a bright loop-top SXR source region. We argue that the magnetohydrodynamic turbulence that appears at the loop apex could be an efficient accelerator of non-thermal particles, which the island structures can trap at the loop-top. These accelerated non-thermal particles can upscatter the surrounding thermal SXR photons emitted by the extremely hot evaporated plasma to HXR photons.

Key words: magnetohydrodynamics (MHD) – Sun: corona – Sun: flares – Sun: X-rays, gamma rays

Supporting material: animation

1. INTRODUCTION

Solar flares, the most powerful events of solar activity, are thought to be the result of magnetic reconnection occuring in the corona and can release in excess of 10^{32} erg of energy in a matter of minutes (Hudson 2011). A substantial fraction of the released energy is transported downwards along the magnetic loop by non-thermal particles (Brown 1971), or by thermal conduction (Fletcher et al. 2011) and/or Poynting flux (Fletcher & Hudson 2008). The bulk of the non-thermal particle energy gets deposited in the chromosphere via Coulomb collisions (Brown 1971). This produces hard X-ray (HXR) emission via non-thermal bremsstrahlung primarily at the footpoints of the loops (Hoyng et al. 1981) and is referred to as the thick target model (Brown 1971). The overpressure resulting from the tremendous energy deposit drives an upward mass flow at speeds up to hundreds of kilometers per second, known as chromospheric evaporation. The affected coronal loops thereby get filled with hot plasma and these loops are then observed via thermal soft X-ray (SXR) emission (Veronig et al. 2005). Since the intensity of non-thermal bremsstrahlung depends on the ambient plasma density, HXR emission is usually too weak to occur in the corona, where the densities are generally much lower. Only in a few cases, coronal densities seem to be high enough such that HXR sources can be clearly observed in the corona (e.g., Veronig & Brown 2004). Nevertheless, several examples clearly show HXR emission from coronal sources (Frost & Dennis 1971; Hudson 1978; Masuda et al. 1994; Tomczak 2001; Krucker & Lin 2008). Arguably the most famous example by Masuda et al. (1994) showed an impulsive non-thermal HXR source appearing above thermal SXR loops, and this confirmed the overlying cusp geometry of the standard solar flare model (Shibata & Magara 2011). Several events similar to the Masuda one have been observed in solar flares (Tomczak 2001; Petrosian et al. 2002; Krucker & Battaglia 2014), and Petrosian et al. (2002) analyzed 18 events with Yohkoh data to conclude that HXR loop-top emission is common to all flares. At the same time, many events with both SXR and HXR coronal sources show less (compared to the Masuda case) separation ($\leqslant$3500 km) between the thermal SXR loops and the coronal HXR source. Many events in a loop filled by chromospheric evaporation even show co-spatial non-thermal emission (Tomczak 2001; Krucker & Lin 2008).

Therefore, the emission mechanism of these essentially co-spatial loop-top HXR events might be different from the Masuda flare, which was interpreted as a partially thick target up in the corona, by injecting non-thermal particles into the cusp of a magnetic trap (Fletcher 1995). Korchak (1971) concluded that an inverse Compton (IC) contribution might sometimes be significant, particularly in the low ambient density conditions relevant to these loop-top HXR events. With an ambient coronal number density of 10^9 cm^{-3}, IC radiation eventually dominates over bremsstrahlung in the 10–100 keV photon energy range (Krucker et al. 2008). Furthermore, these bright, concentrated, loop-top coronal HXR sources show time variation in the order of tens of seconds to minutes and are most prominent during the rise of the thermal emission (Krucker et al. 2008). Therefore, populations of loop-top non-thermal particles which possibly contribute to HXR emission by IC could be accelerated in turbulent plasma conditions, which also helps to trap particles (Turkmani et al. 2006; Krucker et al. 2008). In such cases, the accelerator is then believed to be co-spatial with the coronal HXR source.

In this paper, we propose a model which generates turbulence in the loop top by the Kelvin–Helmholtz instability (KHI). KHI is triggered by the chromospheric evaporation flows from asymmetric flare energy deposition at both loop footpoints. KHI, produced when two fluid flows have a velocity shear across an interface or finite extent region (Chandrasekhar 1961), is able to form vortices which can trigger further fine-scale reconnection and turbulence in a magnetized plasma (Keppens et al. 1999; Baty et al. 2003; Henri et al. 2013). KHI is well studied at fast–slow stream

interfaces in a variety of solar structures (Heyvaerts & Priest 1983; Andries & Goossens 2001), and has even been observed directly in connection with a coronal mass ejection (Foullon et al. 2011), or in solar prominences (Berger et al. 2010). Taking parameters for magnetized jet flows (in a cylindrical flux tube model) on the basis of observations, KHI has been identified as the reason for unstable magnetohydrodynamics (MHD) waves of varying azimuthal mode number ($m = 1$ to $m = 4$), and this is relevant for cool surges (Zhelyazkov et al. 2015) and for active region (EUV) jets (Zhelyazkov et al. 2016). Here, we will demonstrate KHI in a single suddenly footpoint-heated loop.

The paper is then organized as follows. In Section 2 we describe the numerical setup, in Section 3 we show the results of the simulation and discuss the implications, and conclusions are drawn in Section 4.

2. COMPUTATIONAL ASPECTS

2.1. Initial Setup

Our numerical setup, and initial and boundary conditions follow the model in Fang et al. (2015), using a single-fluid MHD plasma description on a two-dimensional (2D) domain of size 80 by 50 Mm (in x–y). We initialize with a linear force-free magnetic field given by

$$B_x = -B_0 \cos\left(\frac{\pi x}{L_0}\right) \sin\theta_0 \exp\left(-\frac{\pi y \sin\theta_0}{L_0}\right),$$
$$B_y = B_0 \sin\left(\frac{\pi x}{L_0}\right) \exp\left(-\frac{\pi y \sin\theta_0}{L_0}\right),$$
$$B_z = -B_0 \cos\left(\frac{\pi x}{L_0}\right) \cos\theta_0 \exp\left(-\frac{\pi y \sin\theta_0}{L_0}\right), \quad (1)$$

with the angle $\theta_0 = 30°$ between the arcade and the neutral line ($x = 0$, $y = 0$) and the horizontal size of our domain setting $L_0 = 80$ Mm. An important difference from the setup in Fang et al. (2015) is that we adopt a higher magnetic field strength of $B_0 = 80$ G, instead of 50 G in Fang et al. (2015). The 80 G value brings our coronal field strength more in line with values found from direct nonlinear force-free field extrapolations in active regions from observed magnetograms (Guo et al. 2016), and is meant to represent a realistic flare loop magnetic field. For the initial thermal structure, we set a uniform temperature of 10,000 K below a height of 2.7 Mm and fix the temperature variation to ensure a constant vertical thermal conduction flux $\kappa \partial T/\partial y = 2 \times 10^5$ erg cm^{-2} s^{-1} above this height, identical to Fang et al. (2015). The initial density is derived from hydrostatic equilibrium with a number density of 1.2×10^{15} cm^{-3} at the bottom. Given such a simplified temperature profile, the choice of the initial thickness of chromosphere 2.7 Mm, together with the bottom density, is empirical limited by the correct parameter range of corona and the demand for a thick target of flare energy input. There is no flow to start with. To obtain a self-consistent thermally structured corona, we augment this setup with a background heating rate decaying exponentially with height, $H_0 = c_0 \exp\left(-\frac{y}{\lambda_0}\right)$, where $c_0 = 10^{-4}$ erg cm^{-3} s^{-1} and $\lambda_0 = 80$ Mm. This heating appears as a source term in the energy equation, and is meant to balance the radiative losses and anisotropic heat conduction related losses of the corona in its equilibrium state. With this initial setup, we integrate the governing MHD equations until the above configuration reaches a quasi-equilibrium state at 144 minutes after initialization, when we reset time to zero. In the remainder of this paper, we only discuss the stage following this relaxation phase. The relaxed state of the system is reached when the maximal residual velocity is less than 10 km s^{-1} in the entire domain. Note that this relaxed state has a fully self-consistent thermodynamic and gravitational stratification established throughout the domain and in the arcade loops. Similar to Moschou et al. (2015), one can compare (see in particular their Figure 2) the obtained temperature stratification in the chromospheric to transition region to commonly used semi-empirical VAL-C atmospheres, with our model extending to far higher coronal regions. Similar to Falewicz et al. (2015), our model includes radiative loss, thermal conduction, and heating as adopted in their 1D hydro models, and contrasts with their 2D MHD model which (a) excluded B_z and v_z components, and (b) focused on viscous effects, rather than radiative. Panels (a) and (b) in Figure 1 show the number density and temperature of the relaxed system, respectively. One can see the transition region height vary along x, at heights of typically a few (4–5) Mm. This height is influenced also by the fixed bottom lower chromospheric number density adopted, here set to 1.2×10^{15} cm^{-3}. The right frame (c) quantifies the corresponding thermal X-ray emission as explained further on, which is completely absent for this relaxed initial state. We use the MPI-parallelized Adaptive Mesh Refinement Versatile Advection Code *MPI-AMRVAC* (Keppens et al. 2012; Keppens & Porth 2014; Porth et al. 2014) with an effective resolution of 1024×640 or an equivalent spatial resolution of 79 km in both directions, obtained through four adaptive mesh refinement levels.

2.2. Triggering Chromosphere Evaporation

The effect of the solar flare is modeled by its chromospheric energy deposit, handled as a finite duration heat pulse located at the loop footpoints. The temporal evolution of the heat pulse is controlled by $f(t)$, a piecewise linear ramping function to add and complete the sudden heating within 180 s. The precise choice of ramping function $f(t)$ should mimic its sudden and brief character: adopting other than piecewise linear behavior leads to similar evolutions. The asymmetric energy input is handled by a function $g(x)$, which sets the ratio of energy deposition at the left footpoint ($x < 0$) to the right footpoint ($x > 0$) to 0.8. Both functions appear in heat pulse functional form $H_1(x, y, t)$ (which is an extra energy source term in addition to the background heating $H_0(x, y)$) specified as

$$H_1 = c_1 \exp(-(y - y_c)^2/\lambda^2) f(t) g(x) \quad \text{if } A(x_1, 0) < A(x, y) < A(x_2, 0) \quad (2)$$

$$A(x, y) = \frac{B_0 L_0}{\pi} \cos\left(\frac{\pi x}{L_0}\right) \exp\left(-\frac{\pi y \sin\theta_0}{L_0}\right), \quad (3)$$

$$f(t) = \begin{cases} t/30, & 0 \leqslant t < 30 \text{ s} \\ 1, & 30 \leqslant t < 150 \text{ s} \\ (180 - t)/30, & 150 \leqslant t < 180 \text{ s} \end{cases} \quad (4)$$

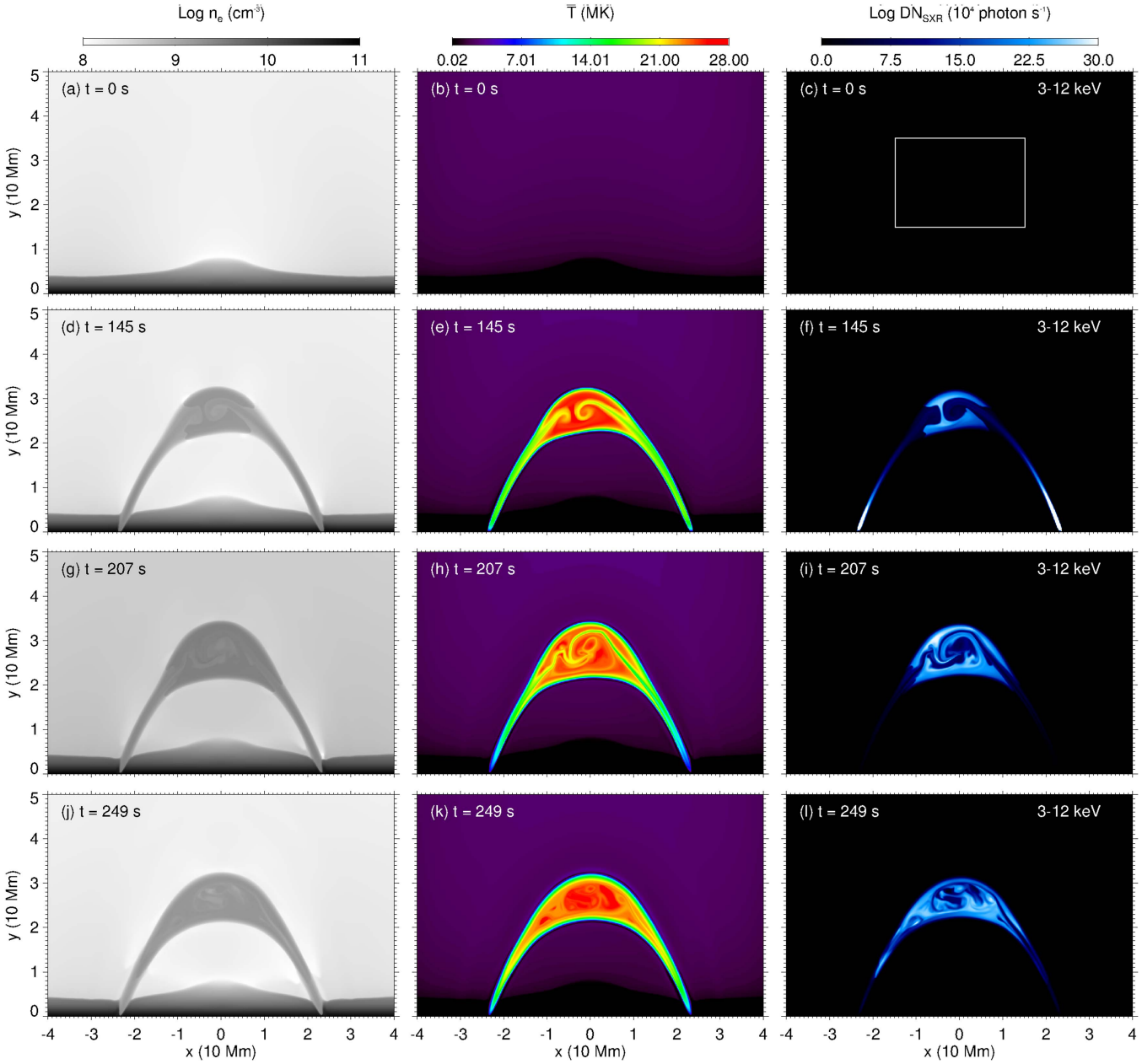

Figure 1. Temporal evolution of number density (left column), temperature (middle column), and synthesized SXR photon flux images (right column) at $t \approx 0$, 145, 207, and 249 s.

(An animation of this figure is available.)

$$g(x) = \begin{cases} 1, & x > 0 \\ 0.8, & x < 0 \end{cases} \quad (5)$$

where $c_1 = 80\,\mathrm{erg\,cm^{-3}\,s^{-1}}$, $y_c = 3\,\mathrm{Mm}$, $\lambda^2 = 10\,\mathrm{Mm}^2$, $x_1 = 24\,\mathrm{Mm}$, and $x_2 = 23\,\mathrm{Mm}$. The heat pulse is located close to the loop footpoint, in the vicinity of the transition region, mimicking the footpoint heating by dissipated non-thermal particles. The energy of H_1 is expected to be quickly transported by thermal conduction away from the footpoints. The extra heating H_1 is active at two footpoints of a single magnetic loop or flux tube consisting of the magnetic field lines identified by the out-of-plane magnetic vector potential component $A(x, y)$ in the range of $x_1 < |x| < x_2$. Panel (a) of Figure 4 shows the resulting temporal evolution of the gas pressure and the adopted heating energy density at the left footpoint (i.e., at $x = -22.5$, $y = 2.5\,\mathrm{Mm}$). We can see that when the footpoint heating H_1 turns on, the gas pressure at the footpoint increases simultaneously from $\approx$0.9 to $\approx$170 erg cm^{-3}. After the heating turns off at $t = 3$ minutes, the gas pressure drops very quickly to $\approx$40 erg cm^{-3}. At $t \approx 5$ minutes, the gas pressure rises again, since then the reflected waves from the apex arrive at this footpoint again.

2.3. Estimating the Thermal X-Ray Emission

We estimate the thermal X-ray emission in the 3–12 keV photon energy range based on the spatial distributions of density and temperature obtained from simulation by the method described in Pinto et al. (2015) and also implemenetd

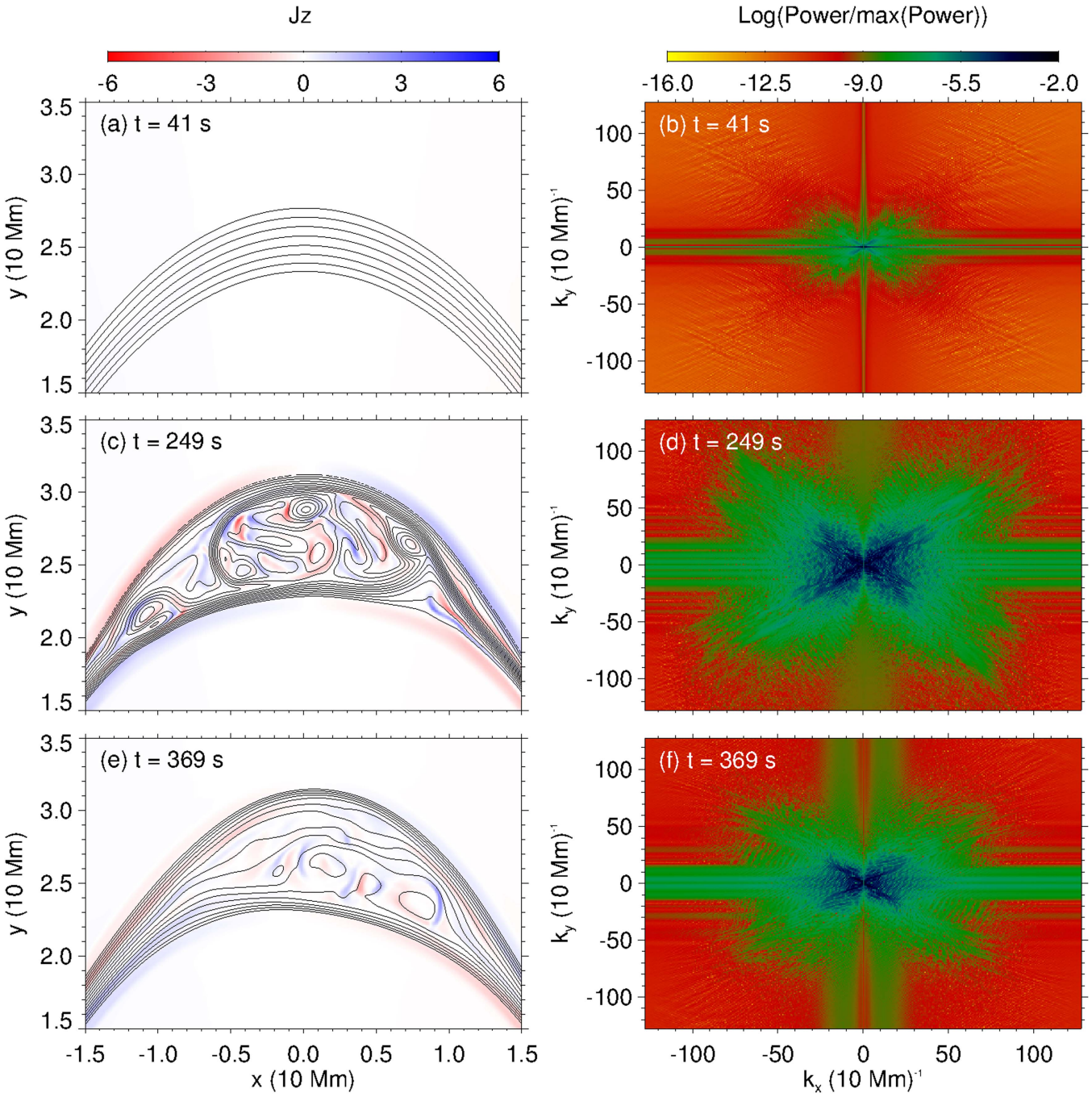

Figure 2. For the region in the white rectangle in panel (c) of Figure 1, the temporal evolution of the current J_z perpendicular to the plane, overlaid by contours of magnetic vector potential (left column), and log-scaled power spectrum from Fourier analysis of the J_z images (right column) at $t \approx 41$, 249, and 369 s.

in the open source forward modeling code FoMo available at https://wiki.esat.kuleuven.be/FoMo. The corresponding continuum thermal X-ray photon flux density of a fully ionized hydrogen plasma emitted at the photon energy $h\nu$ is defined as

$$I(h\nu, T) = I_0 \frac{\mathrm{EM}}{h\nu\sqrt{k_b T}} g_{ff}(h\nu, T) \exp\left(-\frac{h\nu}{k_b T}\right), \quad (6)$$

$$g_{ff}(h\nu, T) = \begin{cases} 1, & h\nu \lesssim k_b T \\ \left(\frac{k_b T}{h\nu}\right)^{0.4}, & h\nu > k_b T, \end{cases} \quad (7)$$

where EM is the emission measure $n^2 V$ of a finite volume V of plasma of number density n and temperature T, the coefficient I_0 is 1.07×10^{-42} for a photon flux measured at a distance of 1 au, if the photon flux density is expressed in units of photons $\mathrm{cm}^{-2}\,\mathrm{s}^{-1}\,\mathrm{keV}^{-1}$, and $g_{ff}(h\nu, T)$ is the Gaunt factor for free–free bremsstrahlung emission. We compute the photon flux density at different photon energies for each individual grid cell, and then integrate the total photon flux density as $\mathrm{DN} = \sum I(h\nu, T)\Delta h\nu$ in the $3 < h\nu < 12$ keV photon energy range. We use 0.01 keV as $\Delta h\nu$, meaning 90 bins in total in the $3 < h\nu < 12$ keV energy range. This process leads to the images shown in Figure 1, right column.

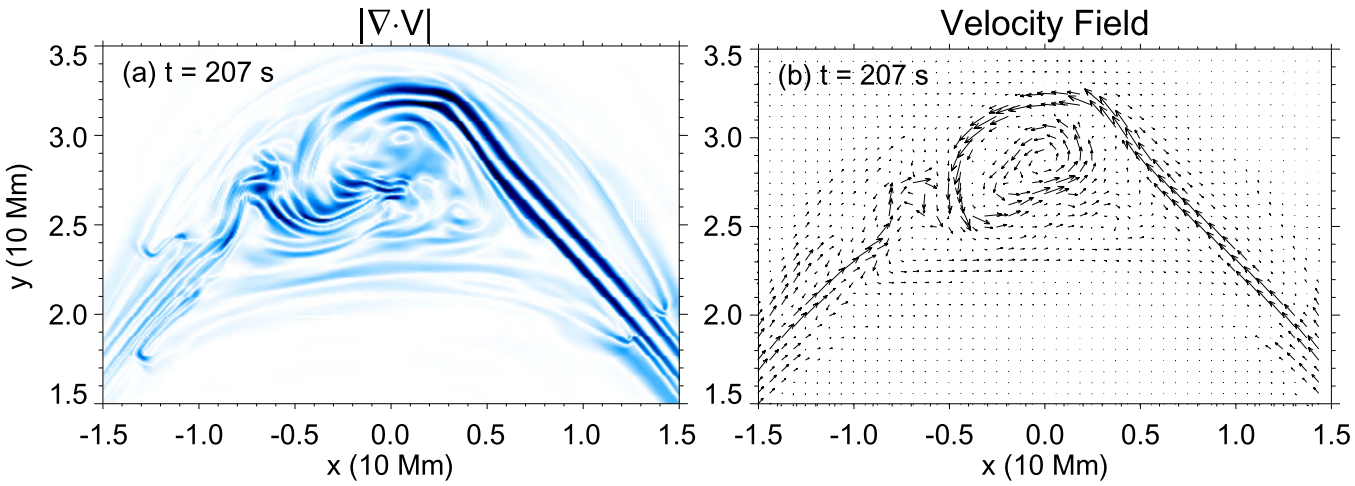

Figure 3. At $t \approx 207$ s, inside the region shown by the white rectangle in panel (c) of Figure 1, we show in panel (a) the absolute value of the divergence of the plasma velocity and the flow field itself in panel (b).

3. RESULTS AND DISCUSSION

3.1. Asymmetric Footpoint Heating Inducing KHI

The temporal evolution of the number density (left column), temperature (middle column), and synthesized SXR photon fluxes (right column) are shown in Figure 1, covering a timespan of about 4.15 minutes. As described in Section 2.2, we use H_1 to mimic the flare energy deposited in the upper chromosphere, and the consequent overpressure resulting from H_1 drives upward mass flows at a speed up to 700 km s^{-1}. We also witness a rapid thermodynamic change (due to thermal conduction) in the loop, reaching an extremely hot temperature around 18 MK. These upward chromospheric evaporation flows have been detected directly in imaging sequences as SXR emission propagating toward the loop-top sources (Silva et al. 1997; Liu et al. 2006; Nitta et al. 2012). This is also seen in our simulation, as in panel (f) of Figure 1 (and in the time period before this image, for which we refer to the corresponding movie). In the last several decades, simulations of chromospheric evaporation have been mostly carried out with symmetric energy input assumptions on both loop footpoints and these focused mainly on the UV-SXR spectral lines produced by the evaporated plasma (Fisher et al. 1985; Mariska et al. 1989; Yokoyama & Shibata 2001; Allred et al. 2005; Liu et al. 2009). However, asymmetric energy deposition at footpoints is a much more likely scenario, and could be intrinsic to the acceleration process as pursued by McClements & Alexander (2005). So, in our simulation we assume that the deposition of flare energy at two footpoints is slightly asymmetric, with a ratio of 0.8 as described in Equation (5). As a result, the right evaporation flow rises quicker and is hotter than the left one as shown in panel (e). Asymmetric energy deposition guarantees that the two evaporation flows will not merely collide at the apex, a situation known to only generate reflected shocks. Panel (e) indeed shows that when our two evaporation flows run into each other asymmetrically, the right one has already crossed the loop apex. In addition, the hotter, right evaporation flow causes a bigger expansion of the loop cross-section in the right half of the loop. This configuration provides the conditions for the formation of shear flows, the trigger of KHI. As shown in panel (e), right after the collision of both flows, KHI begins to develop immediately, and the typical vortical structures of the KHI appear and grow up quickly from panels (e) to (g). The development of vortices in a magnetized plasma can further induce small-scale structure to develop, with a potential cascade of energy to establish a turbulent plasma state (Keppens et al. 1999; Baty et al. 2003; Elmegreen & Scalo 2004; Henri et al. 2013).

The ratio set by $g(x)$ of 1:0.8 for asymmetric heating is not a special choice in terms of KHI development. If this ratio is closer to 1:1, the location where the two evaporation flows from both footpoints collide is closer to the apex, as well as the region prone to KHI. If KHI occurs closer to the apex, we do find that the resulting turbulence life time is extended. If we repeat the simulation with a ratio 1:0.5, the results do not qualitatively change too much. We can even find KHI in the extreme asymmetric case where the ratio is 1:0, meaning only one footpoint is heated. Figure 5 shows the time evolution of this special case. We find that the resulting evaporation flows which are continously driven from one footpoint for a finite duration pulse, also generate KHI, this time when they meet up with the already reflected flows from the other leg of the loop. Similar to Figure 1, the panels in Figure 5 also clearly show turbulence, magnetic islands, and their SXR evolutions, this time on the left loop leg. From this special case, we argue that the causal relationship between asymmetric footpoint heating and KHI is general. We note that the purely symmetric case, as analyzed in Falewicz et al. (2015), is special in that when perfect (numerical) symmetry is maintained, no KHI can develop. An important parameter is the total energy deposited, setting the pressure perturbation (see Figure 4), as well as the location of the deposition near the transition region (Falewicz et al. 2015). Indeed, Srivastava & Murawski (2012) show a slow shock wave propagating between the footpoints of a heated loop due to single footpoint heating, and Fang et al. (2015) also present a similar result, but no KHI has been found then. The reason is that Srivastava & Murawski (2012) obtain a rather slow (30 km s^{-1}) plasma propagation, while Fang et al. (2015) focus on a faster (300 km s^{-1}) case inspired by observations from Kumar et al. (2015). The different results from Figure 5 in this work to our previous work (Fang et al. 2015) are mainly due to the larger energy input here (and the overall field strength). The larger footpoint heating evaporates faster flows which can trigger KHI more easily. So we infer that stronger flares are more likely to generate KHI

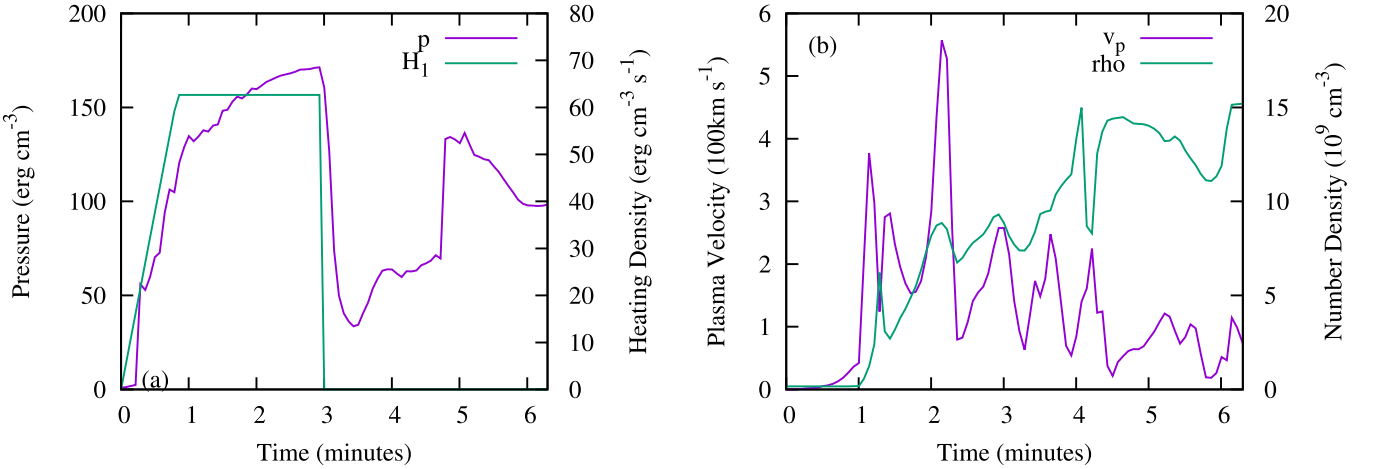

Figure 4. Panel (a) shows the temporal evolution of the gas pressure and the heating energy density at the left footpoint. Panel (b) shows the temporal evolution of the plasma velocity and number density at the apex of the loop.

by driving more energetic, asymmetric chromospheric evaporation.

Our grid-adaptive simulations offer enough resolution to also capture a number of (numerical) reconnection processes occurring during vortex development. The left column in Figure 2 shows the temporal evolution of the current distribution perpendicular to the plane (the component J_z) in a color scale, overlaid with contours of the magnetic vector potential which identify magnetic field lines. By the vortical winding up of the field, we obtain locally anti-parallel magnetic field lines and accompanying strong current sheets, all introduced by the KHI as a trigger for local reconnection processes near the apex as shown in panel (c). The resulting magnetic islands keep evolving, merging, and splitting for the following 4 minutes. In fully kinetic simulations of isolated reconnection layers, Drake et al. (2006) demonstrated that the formation of micro-turbulence inside current sheets can act as a non-thermal particle accelerator. Although we only simulated the MHD scales, the mesoscopic (i.e., in between the macro-scale of the loop diameter and the kinetic scales) current sheets in panel (c) can form micro-turbulence inside them and accelerate particles very efficiently. Normally, in an open magnetic configuration, such high energy particles escape easily in the order of seconds. In that case, the HXR emission which depends on the density of non-thermal particles cannot achieve a high intensity. However, in our simulation, the accompanying rotating magnetic islands exist on MHD scales for several minutes, so they can trap the accelerated particles during their formation at the loop apex. Note that the local island structures indeed have minute-long lifetime and fine-structure variation, which match the timescale and variation suggested by observations for loop-top HXR sources (Krucker et al. 2008). The observations suggest that the time variations of loop-top HXR sources are most prominent during the rise of the thermal emission, normally observed as SXR emission (Krucker et al. 2008). In order to confirm that the chromospheric evaporation flows not only have the ability to trigger KHI to establish the preferred loop-top site for particle acceleration, but also provide enough SXR photons for the IC mechanism producing HXR emission, we calculate the thermal emission of the plasma by the method in Section 2.3 in the energy range of 3–12 KeV, a typical SXR band in *RHESSI*, as shown by the right column in Figure 1. At the initial stage of the flare energy deposition, the SXR emission is concentrated at the two footpoints, and then rises to the apex. Afterwards, the collision between two evaporation flows compresses the plasma at the loop-top area and increases both the number density and temperature there, resulting in a bright loop-top SXR source as shown in panels (f), (i), and (l). The evolution of SXR emission in our simulation not only recovers the previous observational result of SXR emission in flare events (Veronig et al. 2005; Liu et al. 2006), but also indicates the co-spatial and simultaneous relationship between the particle accelerator introduced by the KHI and the generation of SXR photons from thermal emission of hot plasma. Thus, the IC emission mechanism has all the ingredients needed to create an HXR source with time order of minutes at the apex.

Van Doorsselaere et al. (2011) observed both long-period and short-period oscillations during a flare. The long-period oscillation was interpreted in terms of standing slow sausage modes, while the short-period oscillation should be a standing fast sausage mode. Using 1D radiative hydro models, Tsiklauri et al. (2004) point out that asymmetric heating could produce (harmonics of) standing slow mode waves, yielding quasi-harmonic oscillations. Our model is fully 2D, and oscillations can also be seen in the online animated version of Figure 1. When we extract the temporal evolution of plasma velocity and number density in the apex, shown in panel (b) of Figure 4, we can detect variations with a period of around 1 minute in the plasma velocity. However, this oscillation is a mixture of compressible modes, where we can see interfering, propagating waves and oscillations within the developing turbulent structures. The typical period of the slow mode oscillations, which depends also on loop length, is normally longer and more regular in time than the one inside the turbulence. So we infer that the oscillations in panel (b) of Figure 4 from $\approx$1 to $\approx$4.5 minutes are dominated by slow mode oscillations, while after $t \approx 4.5$ minutes, the oscillations present more the characteristics of KHI turbulence. McKenzie & Mullan (1997) and Terekhov et al. (2002) observed quasi-periodic pulsations (QPPs) with long periodicities in the X-ray band in association with a flare, as well as the radio band (Wang & Xie 2000). We suggest that the oscillations on top of the resulting turbulence, the SXR sources (from the hot plasma), and the possible HXR sources (which we argue for based on

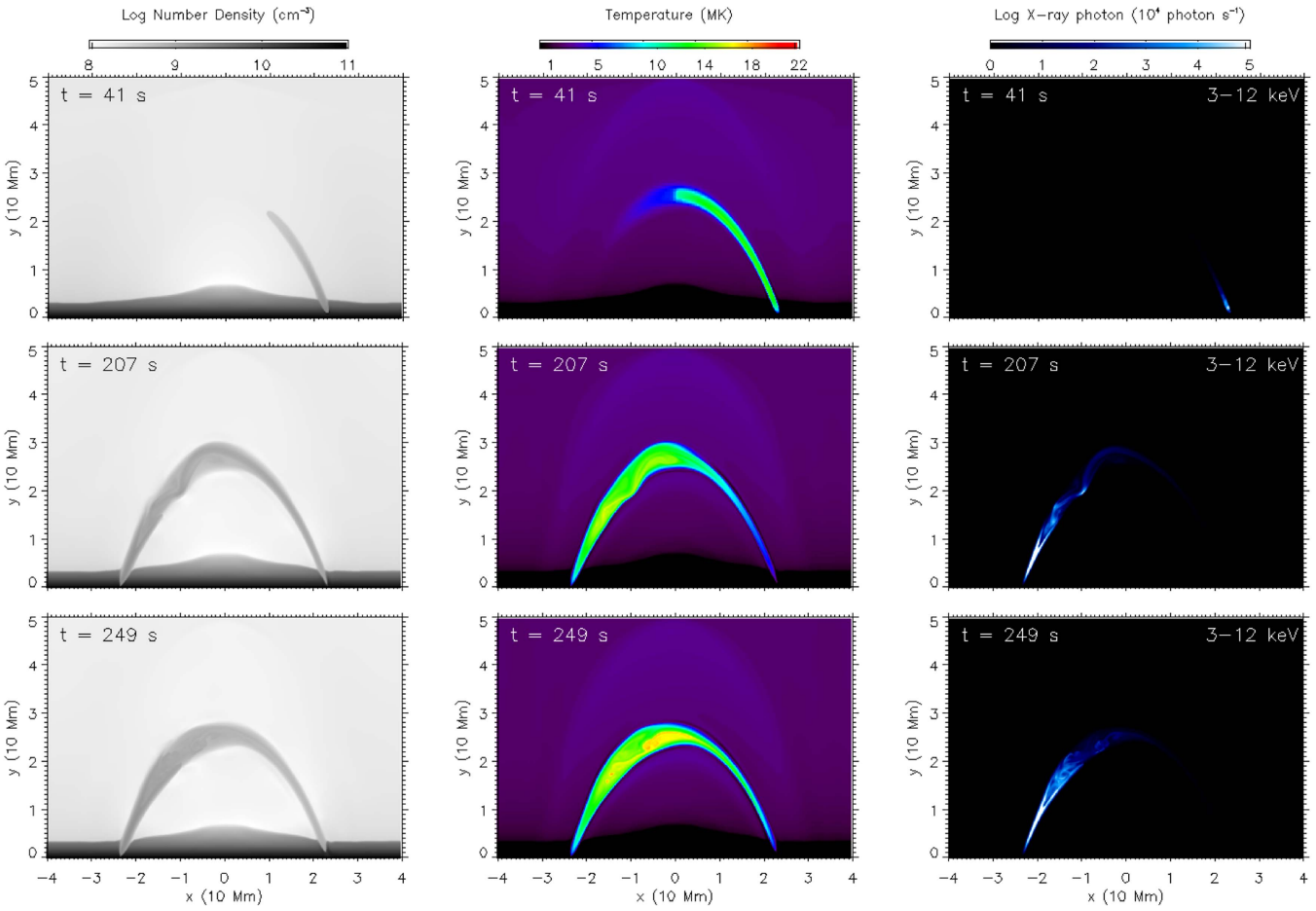

Figure 5. Same as Figure 1, but for the case of strong, single footpoint heating at $t \approx 47$, 207, and 249 s.

our simulation) are consistent with the observations of long period QPPs.

3.2. Ingredients for Non-thermal Particle Acceleration

The exact nature of particle acceleration in flares is still a matter of debate (Fletcher & Hudson 2008; Brown et al. 2009), but our simulation supports the suggestion by Krucker et al. (2008) that loop-top non-thermal particles are very likely accelerated and trapped by localized turbulent plasma. Turbulence is the most natural agent for establishing an energy cascade over a large dynamical range, and the corresponding stochastic acceleration models have been widely used for solar flare studies (Miller 1997; Petrosian & Liu 2004). We find strong indications of KHI induced turbulence at the apex in our simulation. Such turbulence could be a possible accelerator for non-thermal particles. The acceleration mechanism in turbulence is usually first order Fermi acceleration by shocks and second order Fermi acceleration by stochastic processes (Fermi 1949). From our MHD model, we can only argue how shocks and stochastic processes are indeed locally realized. Panel (a) in Figure 3 shows the absolute value of the divergence of the velocity field in the zoomed-in region shown by the white rectangle in panel (c) of Figure 1. This identifies the locations of strong compression, an indication of shock fronts, and suggests that first order Fermi acceleration can take place efficiently there. We also show the flow field itself in panel (b), revealing that the island structures seen in Figure 2 are indeed correlated to vortical flow structures. We interpret the fine-structure seen as (not yet fully resolved) turbulence which infers that stochastic acceleration could also play a part in this region as well.

The efficiency of the acceleration process in turbulence strongly depends on the existence of short wavelength structures (or high wave number components). We perform a spatial Fourier analysis on each frame of $J_z(x, y)$ shown in the left column of Figure 2, by forward fast Fourier transform procedure (FFT, IDL8.2). With shifting the zero-frequency component to the center of the spectrum, FFT implies the transformation

$$F(k_x, k_y) = \frac{1}{NM} \sum_{x=-N/2}^{N/2} \sum_{y=-M/2}^{M/2} J_z(x, y) \times \exp\left(-i2\pi\left(\frac{k_x \cdot x}{N} + \frac{k_y \cdot m}{M}\right)\right), \quad (8)$$

which has zero point symmetry in the wave number domain. We then obtain the corresponding log-scaled power spectrum in the wave number domain in the right column of Figure 2. Before the start of KHI at $t \approx 41$ s, panel (b) shows that the distribution of this power spectrum is more centrally peaked at low wave numbers, in accord with non-existence of small structures then. During the development of KHI at $t \approx 249$ s, panel (d) demonstrates that the distribution of the power spectrum spreads out to the larger wave numbers, indicating that smaller scale structures are generated. After fading of the

shear flows and vortices at $t \approx 369$ s, KHI is suppressed by the magnetic field, and panel (f) highlights that the power spectrum contracts back into the small wave number regime again, meaning that the small structures disappear. The evolution of the power spectrum in the right column of Figure 2 reveals that the KHI does introduce strong turbulence during its evolution at the apex.

4. DISCUSSION AND CONCLUSION

In this paper, we propose a new ingredient to the standard model for solar flares, for the events where one witnesses the formation of (short duration, i.e., up to few minute long) loop-top HXR sources, co-spatial with the SXR. Our model provides further support to the interpretation that these HXR loop-top sources can occur through the IC mechanism scattering the surrounding SXR photons to higher energy. We show that a slight asymmetry between the left–right footpoint deposited energy by non-thermal particles from the reconnection layer developing above the loops is sufficient to establish rapid chromospheric evaporation flows with speeds up to 700 km s^{-1} that are liable to KHI when they meet near the loop apex. As is usual in KHI evolutions in magnetized plasma conditions, vortices form further fine scale structure within, and the turbulence that appears at the apex of loops, could be considered as an efficient accelerator for non-thermal particles. The island structures are ideal sites for trapping non-thermal particles at the loop-top. We show that our model reproduces thermal SXR evolution related to the evaporation flows, as well as establishing a pronounced SXR source region in the loop-top. We suggest that locally accelerated non-thermal particles can easily upscatter these thermal SXR photons to HXR photons. This needs to be further investigated by augmenting the MHD scenario demonstrated here with test particle evolutions to quantify the efficiency of the acceleration process. Our work provides strong support to the role of KHI as a clear trigger of loop-top SXR to HXR emission, during the impulsive phase of single loop flares. In the future, more realistic multiloop configurations as analyzed in Petrosian et al. (2002) must be modeled, and consistent studies of the acceleration processes will need to account for the many types of different and also longer duration HXR events (Krucker & Lin 2008).

The research has been sponsored by an Odysseus grant of the FWO Vlaanderen. The results were obtained in the KU Leuven GOA project GOA/2015-014 and by the Interuniversity Attraction Poles Programme initiated by the Belgian Science Policy Office (IAP P7/08 CHARM). Part of the simulations used the infrastructure of the VSC—Flemish Supercomputer Center, funded by the Hercules Foundation and the Flemish Government—Department EWI. We acknowledge fruitful discussion with Hugh Hudson, Yang Guo and Patrick Antolin.

REFERENCES

Allred, J. C., Hawley, S. L., Abbett, W. P., & Carlsson, M. 2005, ApJ, 630, 573
Andries, J., & Goossens, M. 2001, A&A, 368, 1083
Baty, H., Keppens, R., & Comte, P. 2003, PhPl, 10, 4661
Berger, T. E., Slater, G., Hurlburt, N., et al. 2010, ApJ, 716, 1288
Brown, J. C. 1971, SoPh, 18, 489
Brown, J. C., Turkmani, R., Kontar, E. P., MacKinnon, A. L., & Vlahos, L. 2009, A&A, 508, 993
Chandrasekhar, S. 1961, Hydrodynamic and Hydromagnetic Stability (Oxford: Clarendon)
Drake, J. F., Swisdak, M., Che, H., & Shay, M. A. 2006, Natur, 443, 553
Elmegreen, B. G., & Scalo, J. 2004, ARA&A, 42, 211
Falewicz, R., Rudawy, P., Murawski, K., & Srivastava, A. K. 2015, ApJ, 813, 70
Fang, X., Yuan, D., Van Doorsselaere, T., Keppens, R., & Xia, C. 2015, ApJ, 813, 33
Fermi, E. 1949, PhRv, 75, 1169
Fisher, G. H., Canfield, R. C., & McClymont, A. N. 1985, ApJ, 289, 414
Fletcher, L. 1995, A&A, 303, L9
Fletcher, L., Dennis, B. R., Hudson, H. S., et al. 2011, SSRv, 159, 19
Fletcher, L., & Hudson, H. S. 2008, ApJ, 675, 1645
Foullon, C., Verwichte, E., Nakariakov, V. M., Nykyri, K., & Farrugia, C. J. 2011, ApJL, 729, L8
Frost, K. J., & Dennis, B. R. 1971, ApJ, 165, 655
Guo, Y., Xia, C., & Keppens, R. 2016, ApJ, 828, 83
Henri, P., Cerri, S. S., Califano, F., et al. 2013, PhPl, 20, 102118
Heyvaerts, J., & Priest, E. R. 1983, A&A, 117, 220
Hoyng, P., Duijveman, A., Machado, M. E., et al. 1981, ApJL, 246, L155
Hudson, H. S. 1978, ApJ, 224, 235
Hudson, H. S. 2011, SSRv, 158, 5
Keppens, R., Meliani, Z., van Marle, A. J., et al. 2012, JCP, 231, 718
Keppens, R., & Porth, O. 2014, JCoAM, 266, 87
Keppens, R., Tóth, G., Westermann, R. H. J., & Goedbloed, J. P. 1999, JPlPh, 61, 1
Korchak, A. A. 1971, SoPh, 18, 284
Krucker, S., & Battaglia, M. 2014, ApJ, 780, 107
Krucker, S., Battaglia, M., Cargill, P. J., et al. 2008, A&ARv, 16, 155
Krucker, S., & Lin, R. P. 2008, ApJ, 673, 1181
Kumar, P., Nakariakov, V. M., & Cho, K.-S. 2015, ApJ, 804, 4
Liu, W., Liu, S., Jiang, Y. W., & Petrosian, V. 2006, ApJ, 649, 1124
Liu, W., Petrosian, V., & Mariska, J. T. 2009, ApJ, 702, 1553
Mariska, J. T., Emslie, A. G., & Li, P. 1989, ApJ, 341, 1067
Masuda, S., Kosugi, T., Hara, H., Tsuneta, S., & Ogawara, Y. 1994, Natur, 371, 495
McClements, K. G., & Alexander, D. 2005, ApJ, 619, 1153
McKenzie, D. E., & Mullan, D. J. 1997, SoPh, 176, 127
Miller, J. A. 1997, ApJ, 491, 939
Moschou, S. P., Keppens, R., Xia, C., & Fang, X. 2015, AdSpR, 56, 2738
Nitta, S., Imada, S., & Yamamoto, T. T. 2012, SoPh, 276, 183
Petrosian, V., Donaghy, T. Q., & McTiernan, J. M. 2002, ApJ, 569, 459
Petrosian, V., & Liu, S. 2004, ApJ, 610, 550
Pinto, R. F., Vilmer, N., & Brun, A. S. 2015, A&A, 576, A37
Porth, O., Xia, C., Hendrix, T., Moschou, S. P., & Keppens, R. 2014, ApJS, 214, 4
Shibata, K., & Magara, T. 2011, LRSP, 8, 6
Silva, A. V. R., Wang, H., Gary, D. E., Nitta, N., & Zirin, H. 1997, ApJ, 481, 978
Srivastava, A. K., & Murawski, K. 2012, ApJ, 744, 173
Terekhov, O. V., Shevchenko, A. V., Kuz'min, A. G., et al. 2002, AstL, 28, 397
Tomczak, M. 2001, A&A, 366, 294
Tsiklauri, D., Nakariakov, V. M., Arber, T. D., & Aschwanden, M. J. 2004, A&A, 422, 351
Turkmani, R., Cargill, P. J., Galsgaard, K., Vlahos, L., & Isliker, H. 2006, A&A, 449, 749
Van Doorsselaere, T., De Groof, A., Zender, J., Berghmans, D., & Goossens, M. 2011, ApJ, 740, 90
Veronig, A. M., & Brown, J. C. 2004, ApJL, 603, L117
Veronig, A. M., Brown, J. C., Dennis, B. R., et al. 2005, ApJ, 621, 482
Wang, M., & Xie, R.-x. 2000, ChA&A, 24, 95
Yokoyama, T., & Shibata, K. 2001, ApJ, 549, 1160
Zhelyazkov, I., Chandra, R., & Srivastava, A. K. 2016, Ap&SS, 361, 51
Zhelyazkov, I., Chandra, R., Srivastava, A. K., & Mishonov, T. 2015, Ap&SS, 356, 231